Chapter 3
Dynamic Strain Ageing, Deformation, and Fracture Behavior

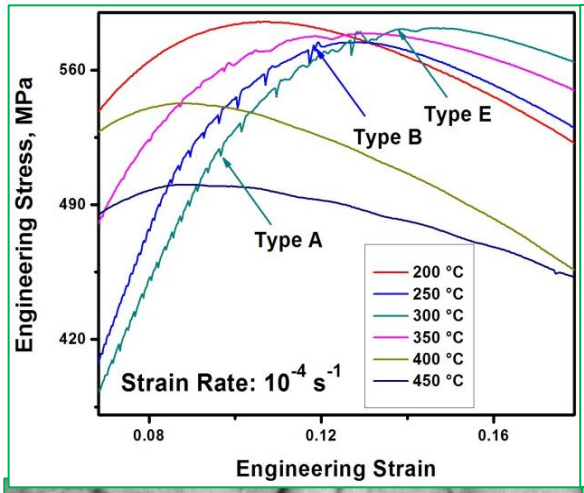

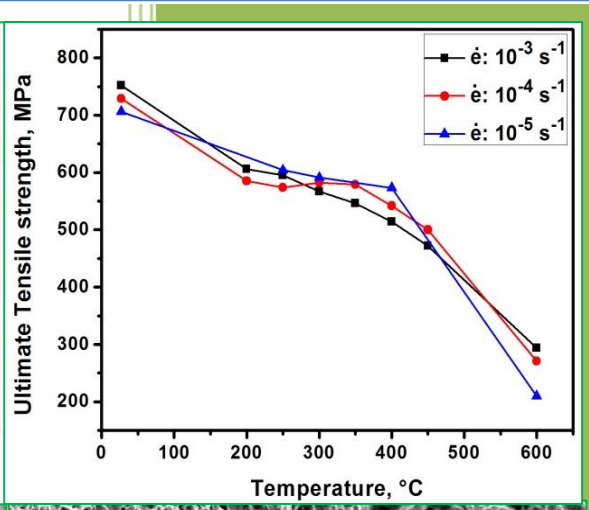

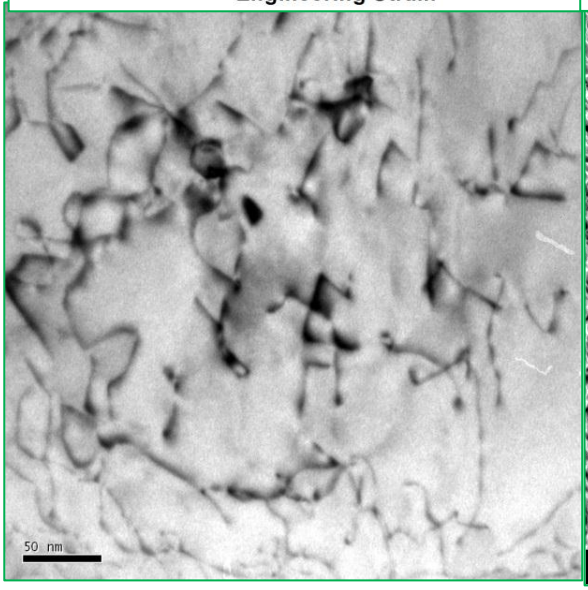

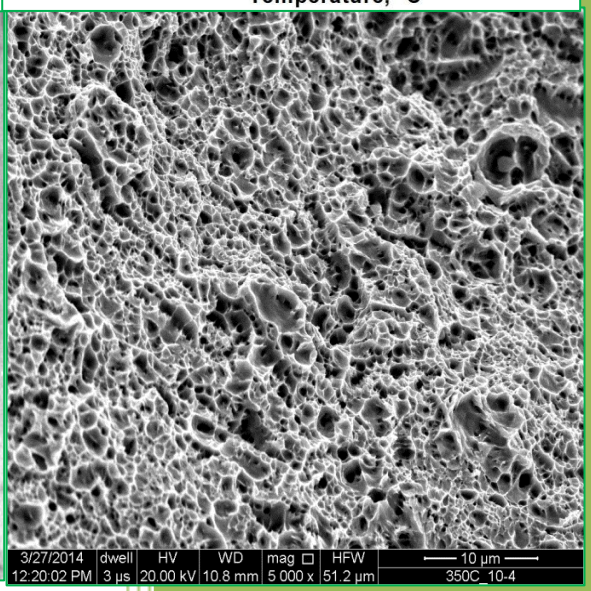

3.1 Introduction

This chapter describes microstructure of the modified 9Cr–1Mo steel in the as received condition (normalized and tempered), tensile behavior at different temperatures and different strain rates and the deformed microstructures. This steel exhibits Dynamic strain ageing (DSA) which is characterized based on serrated flow, plateau/peak in yield and tensile strength, minima in ductility, negative strain rate sensitivity, and peak in internal friction. Dislocation substructures in the region of DSA as well as above and below the region of DSA are presented. Fracture characteristic in the region of DSA are also described.

3.2 Microstructure

Microstructure of the modified 9Cr–1Mo steel in normalized and tempered condition, examined by optical, SEM & TEM is shown in Fig. 3.1. The optical micrograph (Fig. 3.1a) shows microstructure with prior austenite grain boundaries (PAGbs). These grain boundaries decorated with carbide precipitates which are revealed more clearly from the SEM micrograph (Fig. 3.1b).

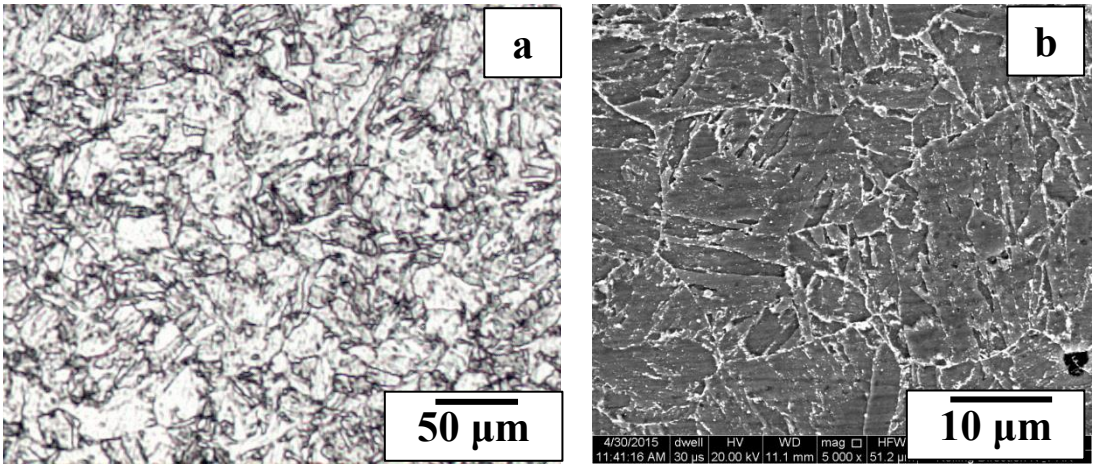

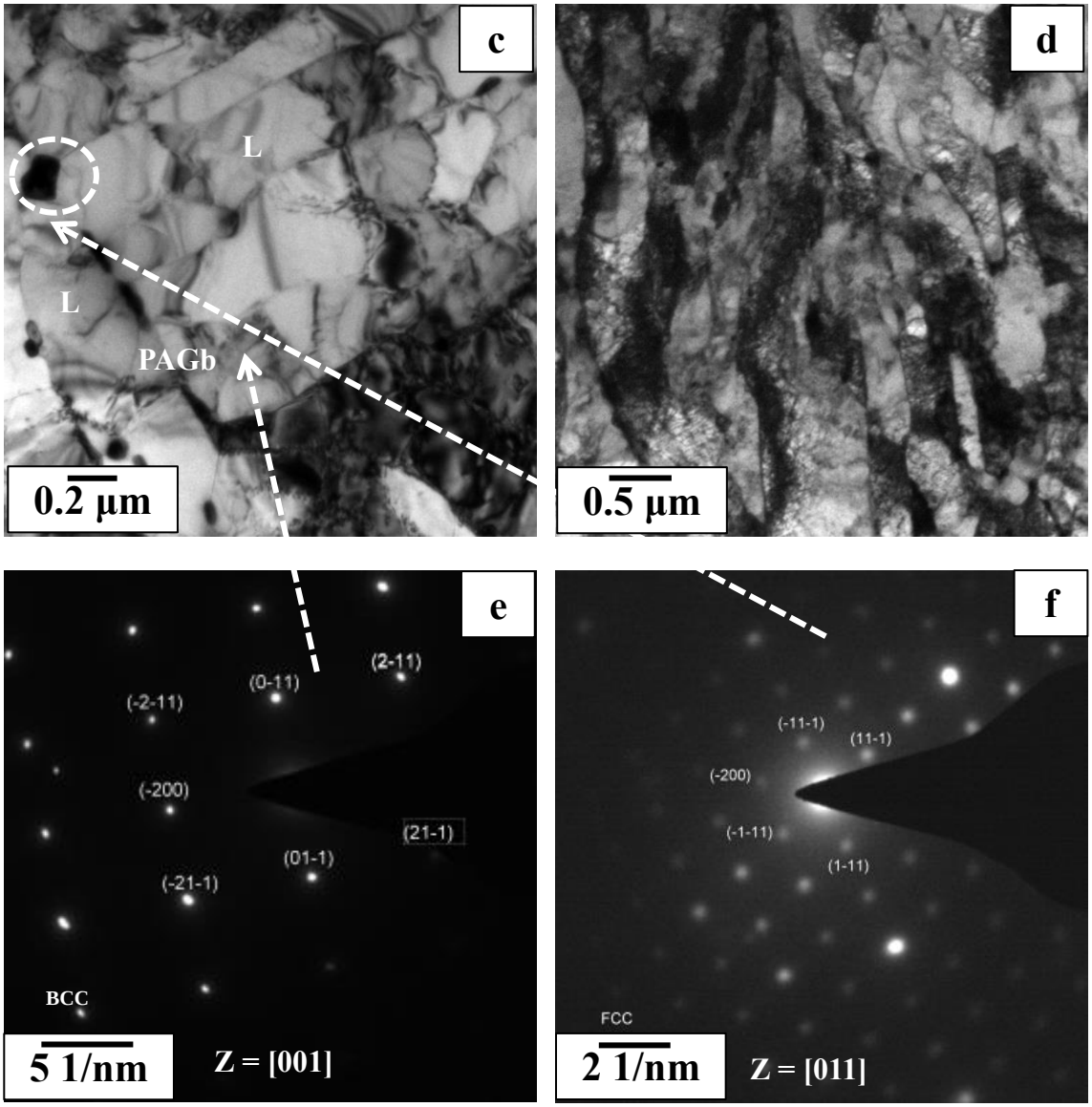

Fig. 3.1 Microstructure of the modified 9Cr-1Mo steel in normalized and tempered condition: (a) optical micrograph, (b) SEM micrograph, (c) TEM micrographs showing laths (L) inside the prior austenite grain boundary (PAGb), carbides along the PAGb, and lath boundary and within the laths, (d) high dislocation density within the laths, (e) diffraction pattern of matrix, and (f) diffraction pattern of the $M_{23}C_6$ carbide encircled in (c).

Second phase particles along the PAGbs and lath boundaries are evident from the TEM micrograph (Fig. 3.1c). Also fine second phase particles are within the laths. In addition to second phase precipitates along the martensite lath boundaries, high density of dislocations may also be seen within the laths (Fig. 3.1d). There are different morphologies of the second phase particles. Crystal structures of the matrix and

precipitates are analyzed from their selected area diffraction (SAD) patterns. Crystal structure of the matrix and precipitates are characterized as *bcc* and *fcc* respectively (Fig. 3.1 e & f). Lattice parameters of different types of precipitates are calculated from their SAD patterns and compared with JCPDS. The cuboidal particles are identified as $Cr_{23}C_6$ carbide with lattice parameter $a \approx 10.65$ Å, the round precipitates as niobium carbide (NbC) with lattice parameter a ≈ 4.47 Å. The rod like precipitates are identified as vanadium carbide (VC). These observations are consistent with earlier findings for this steel in N & T condition [87,88].

3.3. Tensile Properties

3.3.1 Engineering Stress–Strain Curves

Engineering stress–strain curves corresponding to different temperatures, from room temperature (RT) to 600 °C, at different strain rates ($\dot{\varepsilon}$) from 10^{-3} s^{-1} to 10^{-5} s^{-1}, are shown in Fig. 3.2. Serrated plastic flow may be seen in the curves corresponding to test temperatures from 250 to 350 °C at the strain rate of 10^{-4} s^{-1} (Fig. 3.2c), however, there is no serrated flow either at the higher strain rate of 10^{-3} s^{-1} (Fig. 3.2a) or at the lower strain rate of 10^{-5} s^{-1} (Fig. 3.2d). Serrations at low temperature are predominantly of type A; type A + B and E at 300 °C; and type A, E at 350 °C. Further, serrations in the stress–strain curves appear almost from beginning of the plastic deformation and disappear before the attainment of ultimate tensile strength over the temperature range from 250 to 350 °C. The amplitude of serrations increases with increase in strain and the critical strain for the onset of serration also increases with temperature.

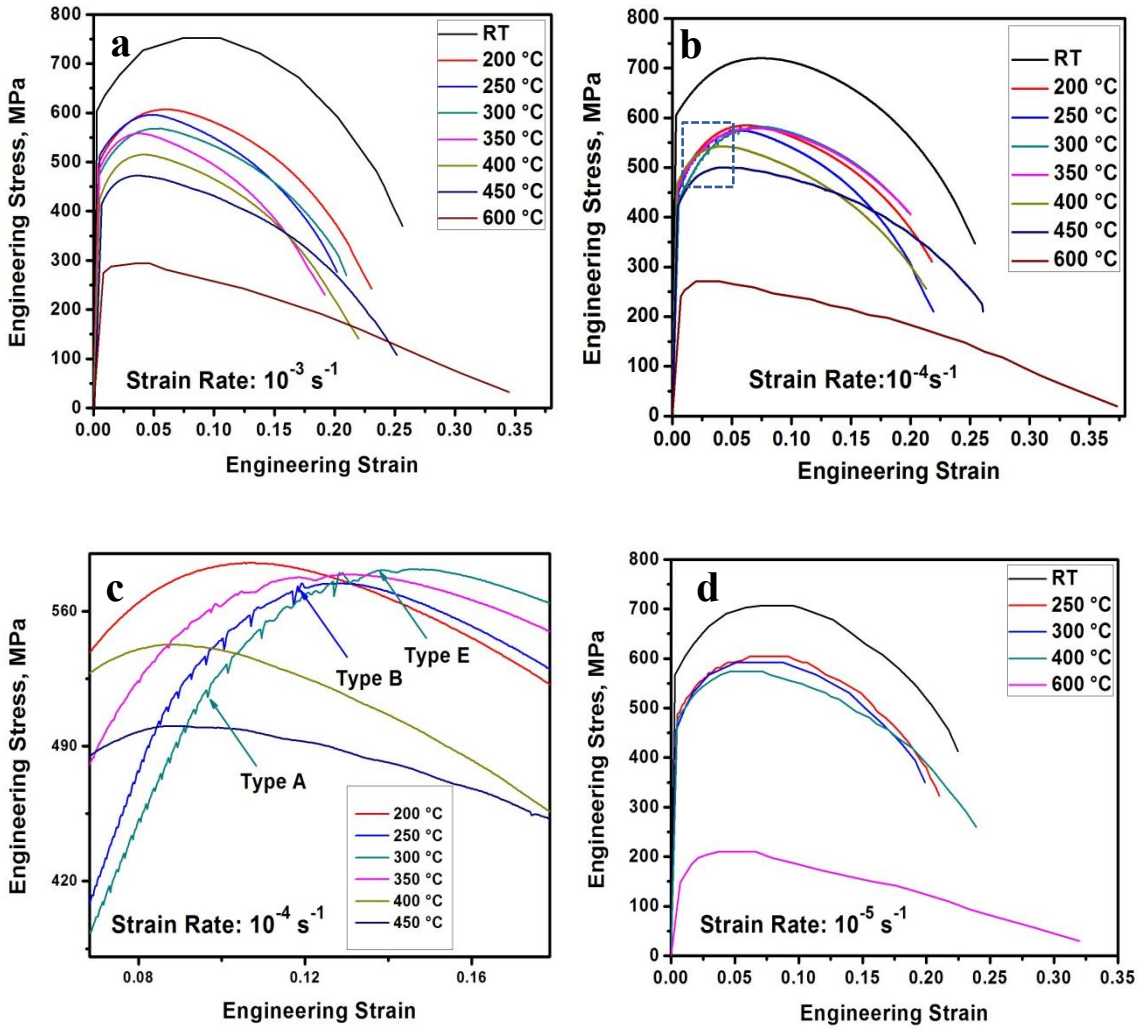

Fig. 3.2 Engineering stress–strain curves corresponding to different temperatures at different strain rates: (a) 10^{-3} s^{-1}, (b) 10^{-4} s^{-1}, (c) magnified view of the portion encircled in rectangular box in the fig. (b), & (d) 10^{-5} s^{-1}.

3.3.2 Variation of Yield Strength and Ultimate Tensile strength with Temperature

The variation of 0.2% offset yield strength with temperature at strain rates of 10^{-5}, 10^{-4} & 10^{-3} s^{-1} is shown in Fig. 3.3a. The yield strength continuously decreases with rise in temperature at high strain rate of 10^{-3} s^{-1} and the rate of fall was relatively lower from 200 to 450 °C. There is a mild peak at 300 °C at the low strain rate of 10^{-5} s^{-1}. On the other hand there is plateau in the plot from 200 to 300 °C and a pronounced peak at 350 °C at the strain rate of 10^{-4} s^{-1}.

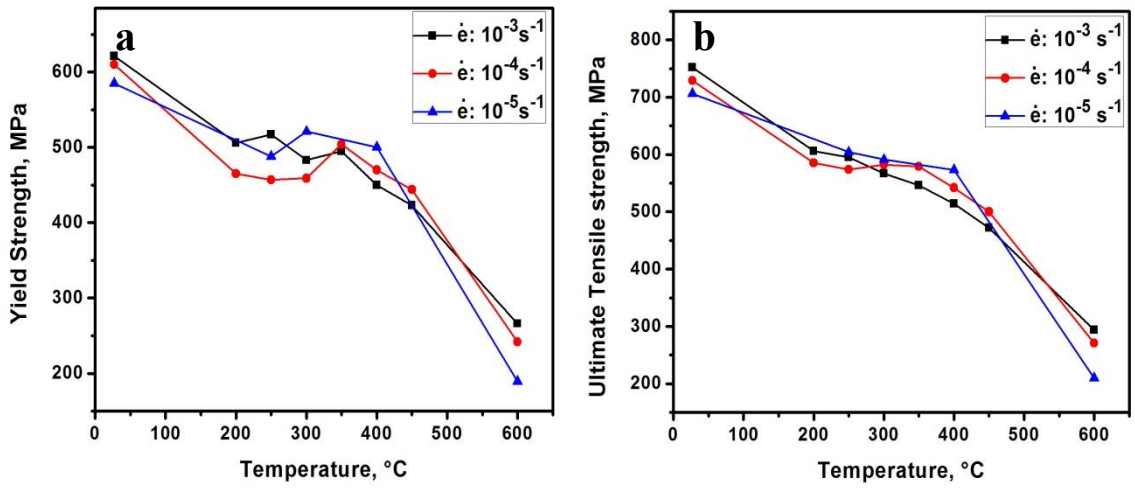

Fig. 3.3 Variation of strength with temperature at different strain rates of 10^{-3}, 10^{-4} & 10^{-5} s^{-1}: (a) yield strength (b) ultimate tensile strength.

The effect of temperature and strain rate on ultimate tensile strength is presented in Fig. 3.3b. Ultimate tensile strength continuously decreases with increase in temperature at the high stain rate of 10^{-3} s^{-1}. There is flattening of the plot over the temperature range from 250 to 400 °C at the strain rate of 10^{-5} s^{-1}. On the other hand there is distinct hump at 350 °C at the strain rate of 10^{-4} s^{-1}.

3.3.3 Variation of Elongation (%) with Temperature

The variation of plastic strain to fracture (e_{pf}) with temperature at different strain rates is shown in Fig. 3.4a. The e_{pf} may be seen to undergo minima in the temperature range 250 to 400 °C. Elongation minimum is found to shift towards the lower test temperature with decrease in strain rate. The uniform plastic strain (e_{pu}) (plastic strain up to ultimate tensile strength) does not show minima rather shows slight increase over the above range of temperature. On the other hand, necking plastic strain (e_{pn}) (strain from maximum tensile stress to fracture stress) shows noticeable minima (Fig. 3.4b).

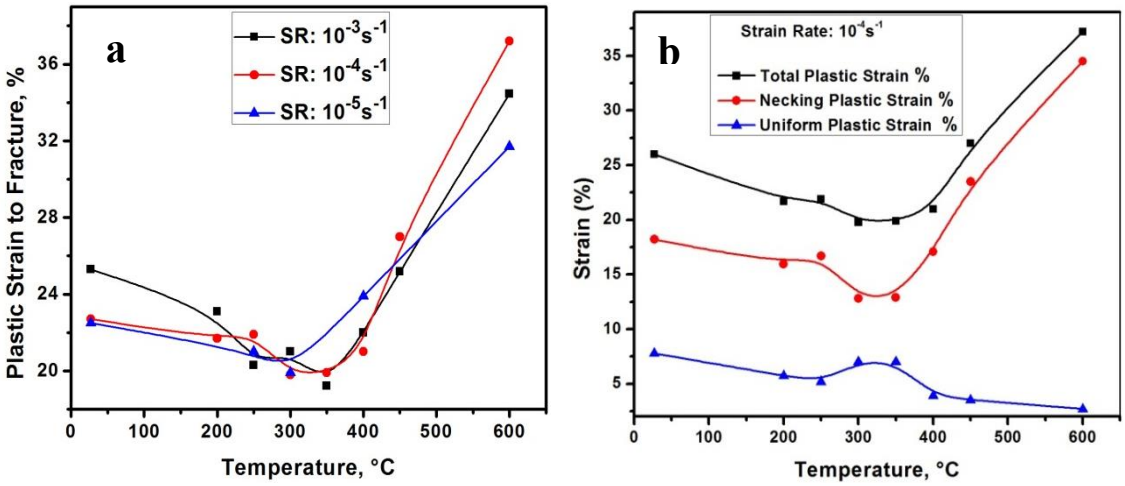

Fig. 3.4 Variation of plastic strain with test temperature: (a) plastic strain to fracture (e_{pf}) at different strain rates, (b) different components of plastic strain (e_{pf}, e_{pu} & e_{pn}) at strain rate of 10^{-4} s^{-1}.

3.3.4 Strain Hardening Exponent

Strain hardening exponent (n) is evaluated from the slope of the log σ vs logϵ_p plot, based on the relationship $\sigma = K{\epsilon_p}^n$, where σ and ϵ_p are true stress and true plastic strain respectively and K is strength coefficient [89]. The variation of n with temperature at different strain rates is shown in Fig. 3.5. While there is continuous drop in n with rise in temperature at the slowest strain rate of 10^{-5} s^{-1}, there is tendency of flattening from 200 to 300 °C at the high strain rate of 10^{-3} s^{-1}. In contrast, a pronounced peak is observed at 300 °C at the intermediate strain rate of 10^{-4} s^{-1}.

Tensile properties at different temperatures at strain rate of 10^{-4} s^{-1} are presented in Table 3.1. The degree of work hardening (UTS/YS) is seen to be highest at 300 °C.

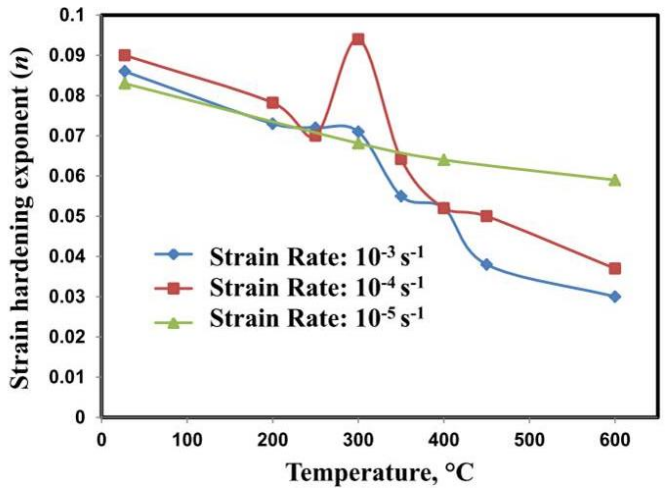

Fig. 3.5 Variation of strain hardening exponent (n) with temperature for the modified 9Cr-1Mo steel at different strain rates of 10^{-3} s^{-1}, 10^{-4} s^{-1} and 10^{-5} s^{-1}.

Table 3.1 Tensile properties at various temperatures at strain rate of 10^{-4} s^{-1}.

Temperature (°C)	Yield Strength (MPa)	Tensile Strength (MPa)	Plastic Elongation to fracture (%)	Uniform Plastic Elongation (%)	Strain Hardening Exponent, n	Strength Coefficient, K (MPa)	Degree of Work Hardening
27	610	729	26.0	8.0	0.090	933	1.205
200	465	585	21.7	5.7	0.078	741	1.258
250	457	574	21.9	5.2	0.070	760	1.256
300	459	582	19.8	7.0	0.094	808	1.267
350	504	579	19.9	7.0	0.064	724	1.148
400	470	542	21.0	3.9	0.052	680	1.153
450	444	500	27.0	3.5	0.050	632	1.126
600	242	271	37.2	2.7	0.037	380	1.119

3.3.5 Strain Rate Sensitivity

Strain rate sensitivity index (m), a measure of dependence of flow stress on the rate of loading/straining, is determined from the slope of the log σ vs log $\dot{\varepsilon}$ plot, based on the relationship $\sigma = c\dot{\varepsilon}^{m}$, where σ and $\dot{\varepsilon}$ are true stress and true strain rate

respectively [89]. The variation of *m* with temperature, based on yield and tensile strength, is shown in Fig. 3.6 a & b respectively.

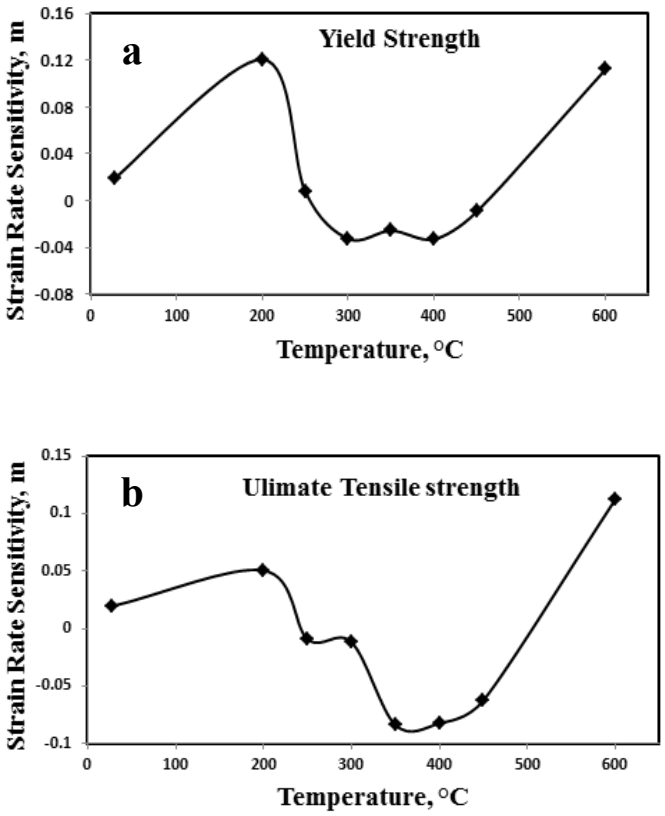

Fig. 3.6 Variation of strain rate sensitivity with temperature based on: (a) yield strength, (b) tensile strength.

It may be seen that *m* does not increase monotonically with temperature. Strain rate sensitivity is found to be negative in the temperature range 250 to 450 °C.

3.3.6 Activation Energy

The activation energy of the process of DSA is evaluated using the relationship $\dot{\varepsilon} = A \exp(-\frac{Q}{RT})$, where $\dot{\varepsilon}$ is true strain rate and Q is activation energy [90]. Q is determined from the slope of the $\ln\dot{\varepsilon}$ vs 1000/T K^{-1} plot, with temperature corresponding

to minimum ductility, at different strain rates (Fig. 3.7). Activation energy is determined to be 58 kJ/mol.

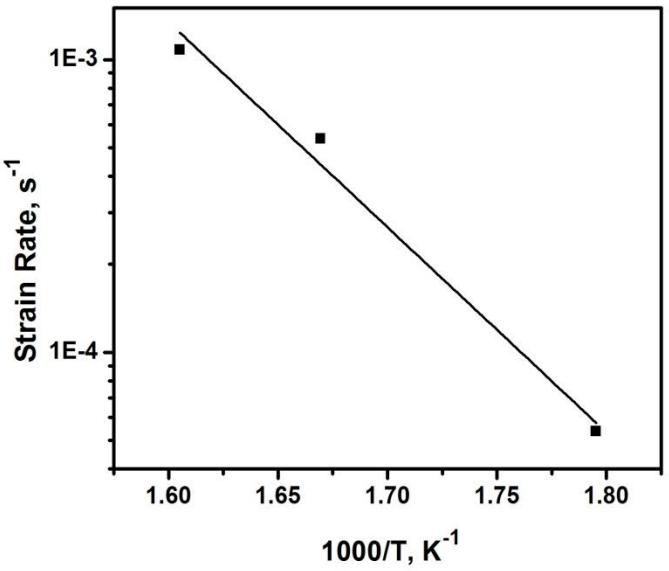

Fig. 3.7 Variation of ln$\dot{\varepsilon}$ with reciprocal test temperature.

3.4 Microhardness

Microhardness of the tensile specimens tested at different temperatures is measured on their transverse sections, about 4 mm below the fractured end. The variation of microhardness with test temperature is shown in Fig. 3.8. It may be seen that there is increase in microhardness of the specimens tested over the temperature range 250–350 °C. The increase in microhardness is most pronounced in the specimen tested at the intermediate strain rate of 10^{-4} s^{-1}.

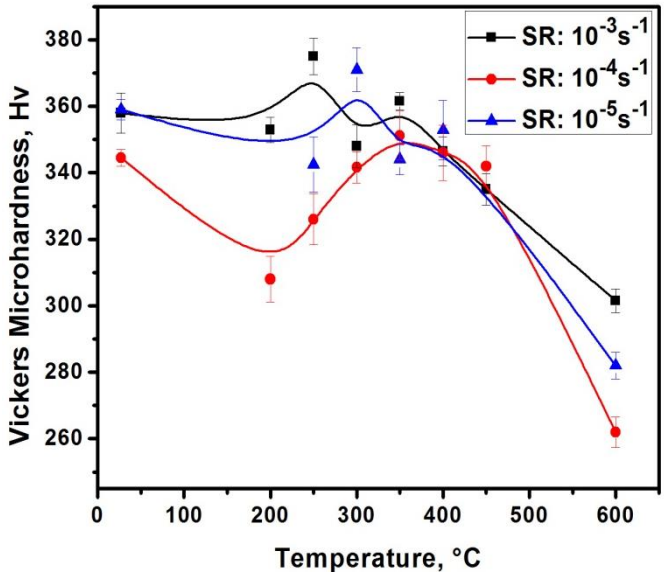

Fig. 3.8. Variation of Vickers microhardness of tensile specimens tested at different temperatures and strain rates.

3.5 Deformation Behavior

The dislocation substructure and slip behavior of the specimens tested over three temperature range: (1) below the region of DSA (RT and 200 °C), (2) in the region of DSA (250 and 350 °C) and (3) above the region of DSA (450 °C), at stain rate of 10^{-4} s^{-1}, are characterized. Dislocation configurations of the specimen tested at RT are shown in Figs. 3.9 a & b. It may be seen that there is uniform distribution of high density tangles of dislocations in different laths (Fig. 3.9a). High dislocation density at the lath boundary and around carbide particles inside the lath are revealed at higher magnification (Fig. 3.9b).

Dislocation substructure resulting from testing at 200 °C is shown in Fig. 3.10. There is formation of subgrains from rearrangement of dislocations in to cells (Fig. 3.10a), an average cell size is found to be of approximately 0.4 μm. Dislocation arrangement within the lath shows uniform array of straight dislocations (Fig. 3.10b).

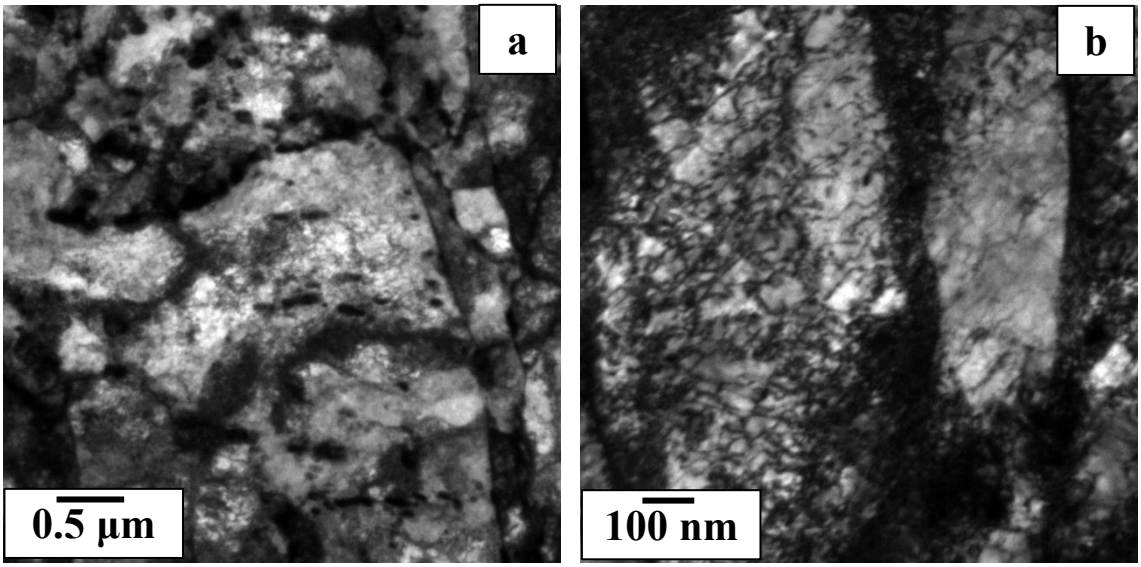

Fig. 3.9 Dislocation substructure below the region of DSA, at RT, at strain rate 10^{-4} $s^{-1.}$

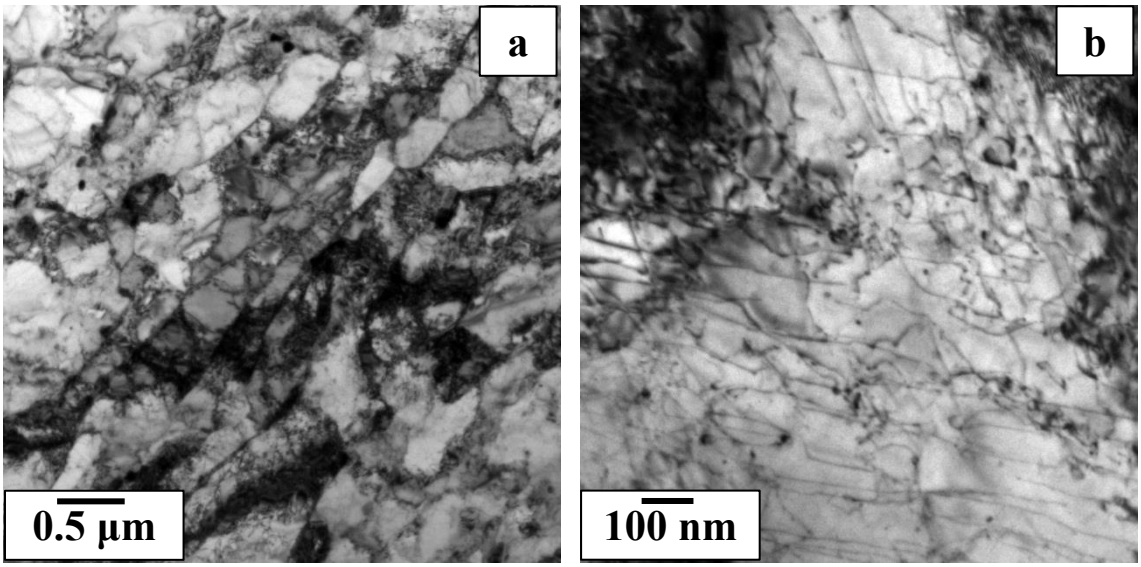

Fig. 3.10 Dislocation substructure below the region of DSA, at 200 °C, at strain rate 10^{-4} s^{-1}.

Bright field TEM micrographs of dislocation substructure developed in the region of DSA, at test temperatures of 250 and 350 °C, are shown in Figs. 3.11 & 3.12 respectively. There is formation of dislocation cell structure also at 250 °C, however, the cell size is decreased to 0.25 μm. Dislocation configuration inside the lath shows

fine dislocation debris and high dislocation-dislocation interaction (Fig. 3.11a). There is significant increase in density of dislocations within the cells as compared to that tested at 200 °C.

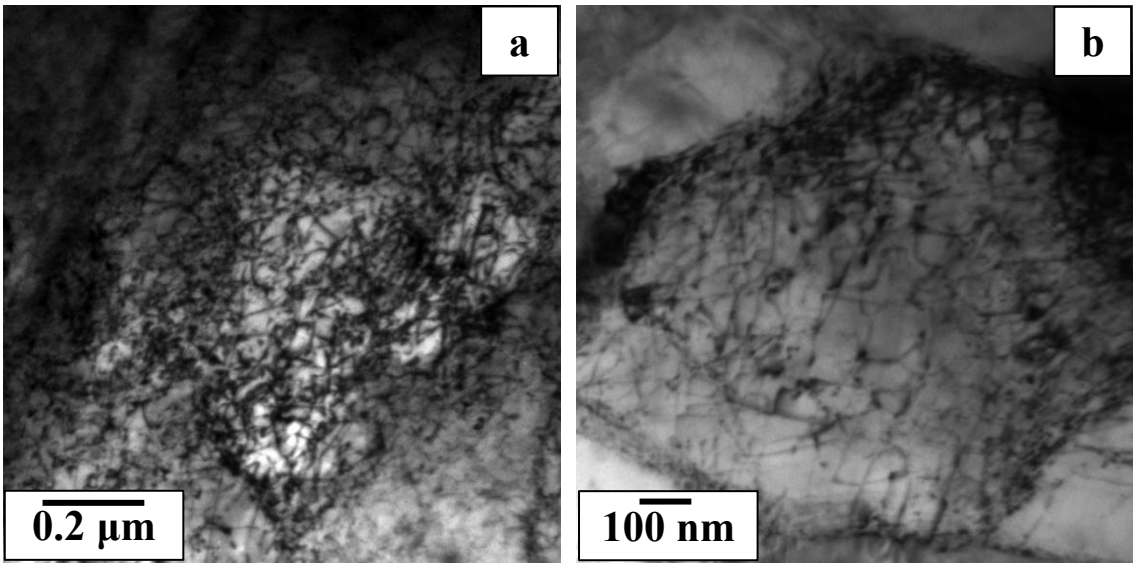

Fig. 3.11 Dislocation configuration in the region of DSA, at 250 °C, at strain rate 10^{-4} s^{-1}.

Dislocation substructure developed at the temperature of 350 °C is shown in Fig. 3.12. The significant increase in dislocations density is obvious from Fig. 3.12a. There is increase in the cell size from 0.25 to 0.54 μm at this temperature compared to that at 250 °C. Formation of dislocation loop and bowing of dislocations (shown by arrows) resulting from pinning of dislocations may clearly be seen in Figs. 3.12 a & b.

Bright field TEM images of dislocation substructure in the specimen tested at 450 °C, above the region of DSA, is shown in Fig. 3.13. There is also formation of dislocation cells with average cell size of 0.57 μm (Fig. 3.13a). Dislocations inside the laths shows array of long and straight dislocations (Fig. 3.13b), which reflects easy movement of dislocations and manifests lowering of yield strength.

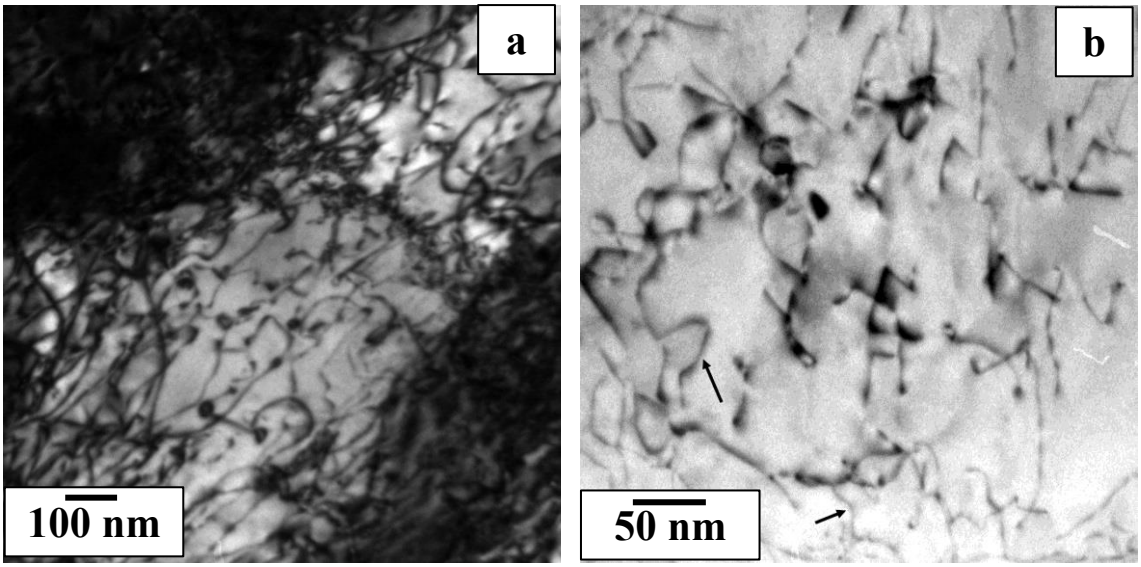

Fig.3.12 Dislocation configurations developed in the region of DSA, at temperature of 350 °C, at strain rate 10^{-4} s^{-1}.

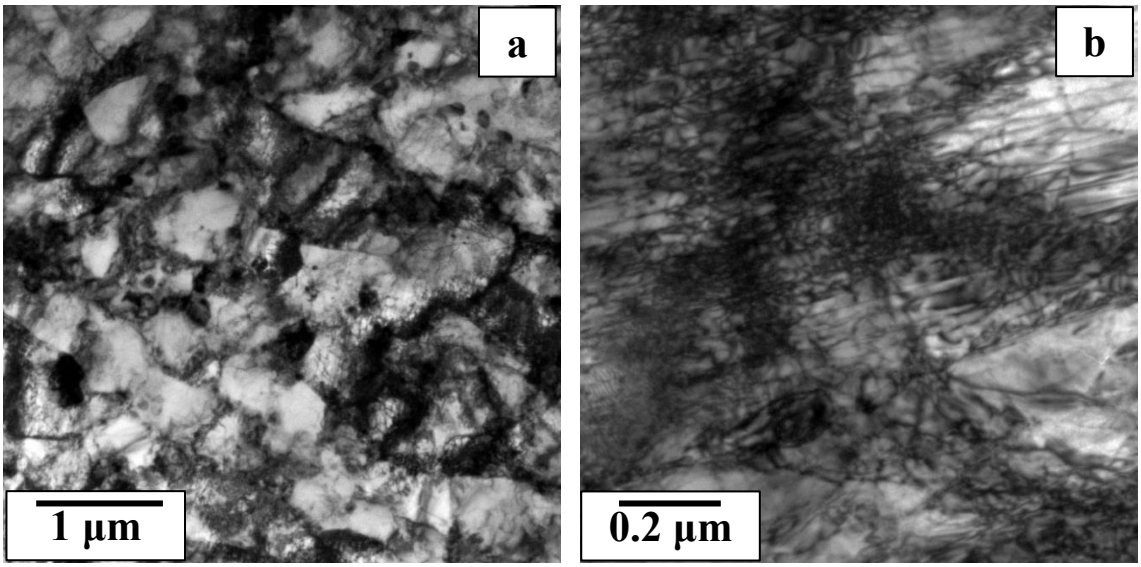

Fig. 3.13 Dislocation configurations developed at 450 °C, above the region of DSA, at strain rate 10^{-4} s^{-1}.

3.6 Fracture Behavior

SEM fractographs of the specimens tested at various temperatures (RT, 200, 350, 450 and 600 °C), at strain rate of 10^{-4} s^{-1}, are displayed in Figs. 3.14–3.16. It is

obvious from these fractographs that there is significant difference in fracture behavior of the material tested from RT to elevated temperature of 600 °C. At RT the fracture is like rosette, consisting of a small fibrous central zone, large intermediate radial zones like flower petals and a very small shear–lip zone at the periphery (Fig. 3.14a). Magnified view of the central fibrous zone revealed fine dimples and large number of faceted features (Fig. 3.14b).

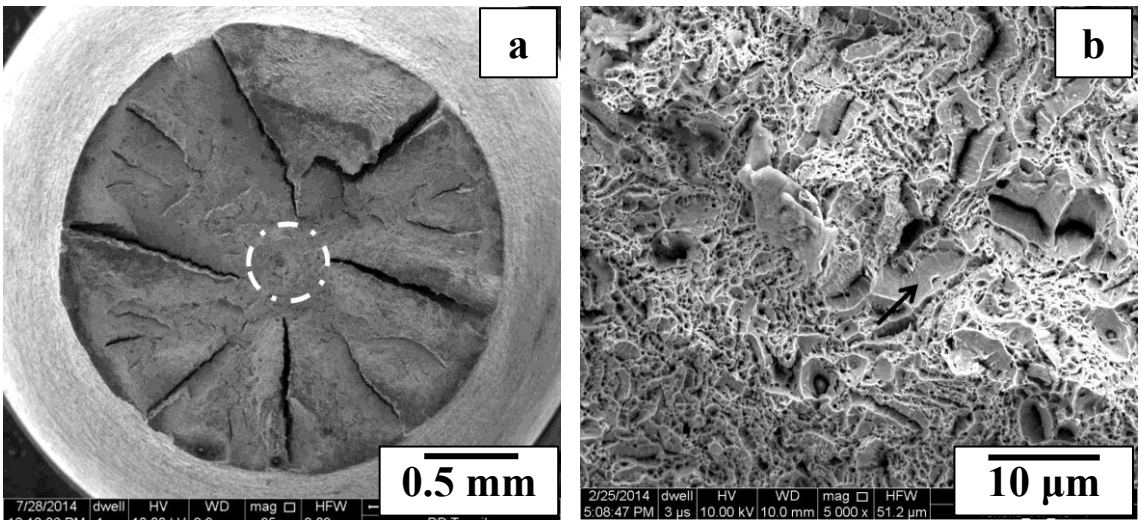

Fig. 3.14 Fractographs of the specimen tested at RT at strain rate 10^{-4} s^{-1}: (a) full view, (b) magnified view of central region (Arrow indicates faceted regions).

On the other hand, at elevated temperatures, from 200–450 °C, there is no longitudinal splitting, rather there are double shear lip zones around the central fibrous zone (Fig.3.15 a–c). The extent of primary shear lip zone is found to decrease with increase in test temperature. The contour of double shear lip zone disappears and there is usual cup and cone fracture at 600 °C (Fig. 3.15d).

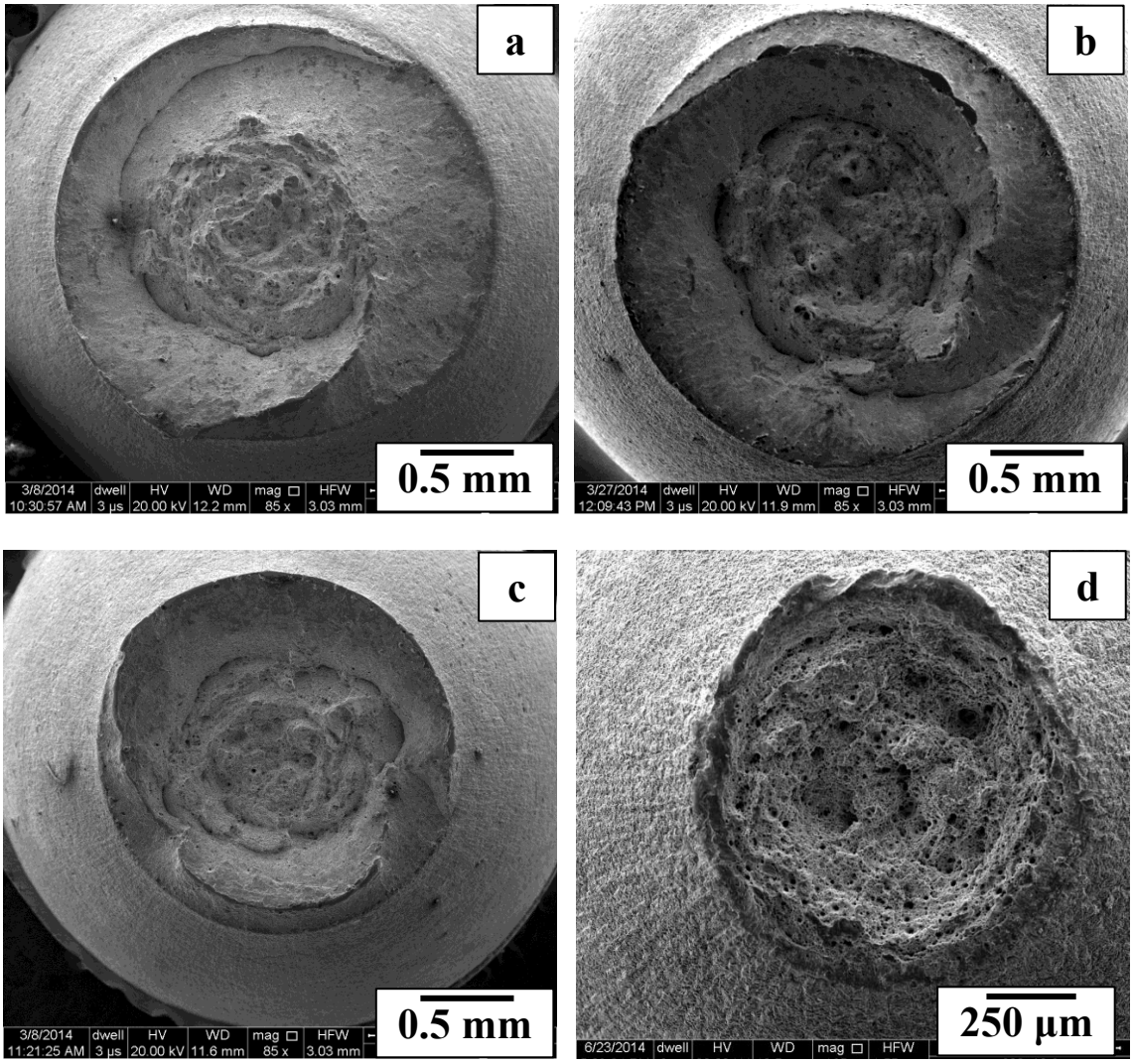

Fig. 3.15 Fractographs showing fracture surfaces of the specimens tested: (a) 200 °C, (b) 350 °C, (c) 450 °C, (d) 600 °C at strain rate 10^{-4} s^{-1}.

Magnified views of central fibrous zones of the specimens tested at 200, 350, 450 & 600 °C are shown in Fig. 3.16 a–d. Equiaxed dimples of varying sizes are observed in fibrous zones of the specimens tested at different temperatures from 200–400 °C. Also there are some flat regions on fracture surface of the specimen tested at 200 °C (Fig. 3.16 a). The size of dimples is smaller in the specimen tested at 350 °C than in that tested at 200 °C. The size of the dimples in the specimen tested at 450 °C is larger (Fig. 3.16c) than those tested at 300 & 350 °C. The size of the dimples is largest in the specimen tested at 600 °C (Fig. 3.16d).

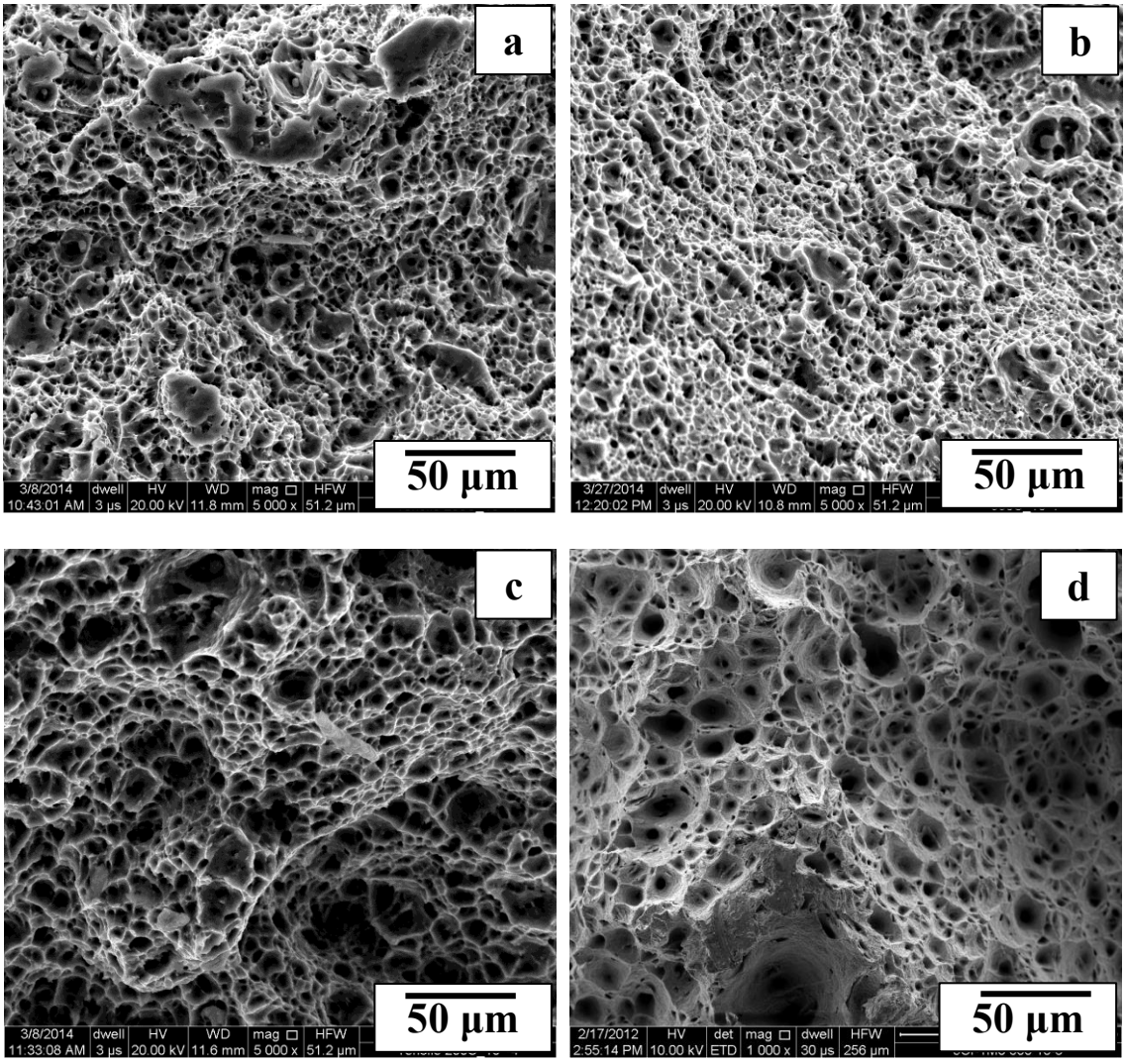

Fig. 3.16 Fractographs of the fibrous zones of the specimens tested at: (a) 200 °C, (b) 350 °C, (c) 450 °C, (d) 600 °C at strain rate of 10^{-4} s^{-1}.

3.7 Internal Friction

Occurrence of Snoek peak in the plot of internal friction vs temperature has been observed by several investigators in the region of DSA in various materials; like austenitic stainless steel 316 [91], nickel base super alloys Inconel 600 and 690 [92] and zirconium–hydrogen alloy [93]. In general, there are two types of sites, octahedral and tetrahedral in bcc lattice which may be occupied by interstitial solute atoms. The defect symmetry sites with respect to surrounding atoms show that both octahedral and tetrahedral sites exhibit tetragonal symmetry [94,95]. Solute atoms induce elastic

dipoles with tetragonal symmetry. The stress induced reorientation of interstitial atoms representing elastic dipoles gives rise to a mechanical loss peak, called Snoek peak. The stress induced reorientation produces anelastic relaxation and is elementary step of interstitial diffusion. Mechanical loss spectra indicate presence of interstitial atoms by Snoek peaks at specific temperatures. Peak height and its position in respect of temperature may vary depending on the chemical composition, distribution of interstitial atoms in the lattice and the degree of cold work [91,95].

Temperature dependency of internal friction in the modified 9Cr–1Mo steel in the normalized and tempered as well as 5% and 10% of cold worked conditions is shown in Fig. 3.17. Two well defined peaks, one between 100–250 °C and the other between 300–450 °C may be seen. A three–fold increase in Snoek peak height is obvious in the region of DSA in comparison with peak in the lower temperature range, suggesting strong interaction between diffusing interstitial atoms and dislocations in this temperature range.

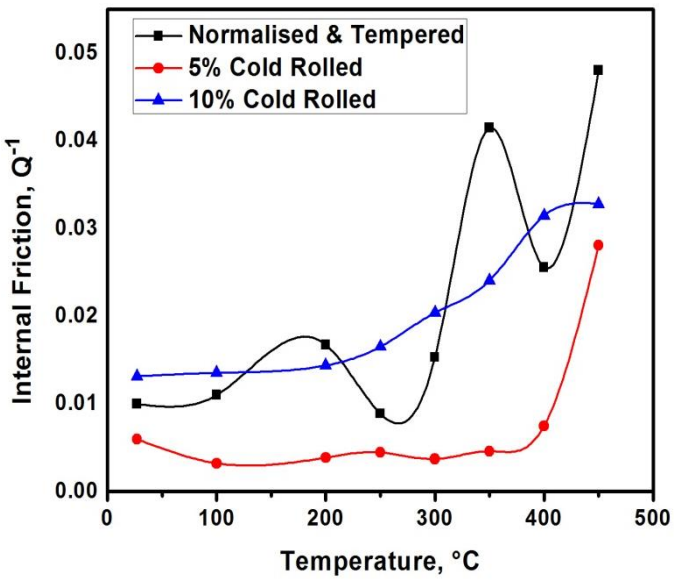

Fig. 3.17 Variation of internal friction of the modified 9Cr–1Mo steel with temperature in normalized & tempered and, 5% and 10% cold rolled condition.

In the 5% and 10% cold worked conditions, the lower temperature peak is found to almost disappear and there is significant increase in internal friction above 400 °C (Fig. 3.17). It may thus be inferred that the 2nd Snoek peak in the cold worked condition would have shifted towards higher temperature.

3.8 Discussion

3.8.1 Dynamic Strain Ageing

3.8.1.1 Tensile Behavior

Serrated plastic flow in the engineering stress–strain curves, over the temperature range from 250–350 °C, at strain rate of 10^{-4} s^{-1}, suggests occurrence of DSA (Fig. 3.2c). In addition to serrated plastic flow, typical characteristic features of DSA like plateau and hump are observed in the curves showing dependence of yield and tensile strength, over the temperature range 250–400 °C. Thus, the temperature range of DSA in this material is established as 250–400 °C, in agreement with the earlier observations [96,97].

DSA behavior of this steel has been studied by several investigators [96,97] and occurrence of type A, B serrations has been reported in the temperature range from 225–425 °C. Occurrence of type A and B serrations, observed in the present investigation, is in accord with the earlier observations [96,97], however, there is slight difference in the range of temperature of DSA reported by the earlier investigators. Serrated yielding is exhibited from diffusion of solute atoms to sites of gliding dislocations, to keep the system in equilibrium, forming solute atmosphere around dislocation core. This interaction between dislocations and solute atoms causes temporary arrest of dislocations in the path of slip [46,91,98,99]. Activation energy of the process of DSA in this steel is determined 58 kJ/mol which lies in the range of 0.4–0.7 times of the activation energy for diffusion of nitrogen in α–iron (80 kJ/mol).

Thus, the phenomenon of DSA in this steel may be attributed to interaction of dislocations with nitrogen atoms, in agreement with the earlier investigations [50,53,56] but in contradiction to the hypothesis of dislocation interaction with carbo–nitrides [97]. It is also worth mentioning that there is difference in the activation energy determined in the present investigation and that reported in the literature. The activation energy reported by several investigators for ferrtic/martensitic 9Cr–1Mo steels is displayed in Table 3.2.

Activation energy for DSA determined in the present investigation is marginally higher than that reported by Kishore et al. [53] for the modified 9Cr–1Mo steel and it is relatively lower than that reported by Choudhary et al. [100–102] for the conventional 9Cr–1Mo steel. DSA behavior of 316L has been studied by Kim et al. [103] varying its nitrogen content, and activation energy for the DSA was found to increase with nitrogen content. Roy et al. [50] have reported increase in activation energy with increase in silicon content in the modified 9Cr–1Mo steel. It may thus be understood that the difference in activation energy between those reported in literature [53] and in the present investigation is due to higher content of nitrogen in the steel of present investigation.

Serrated flow is found to disappear beyond UTS at all the test temperatures. Kishore et al. [56] studied appearance and disappearance of serrations in modified 9Cr–1Mo steel and observed that disappearance was mainly due to diffusion of nitrogen from dislocations to precipitate sinks, causing fall in nitrogen content of the matrix below the critical concentration required to sustain the serrated flow. Generation of high density of dislocations and consequent increase in work hardening in the region of DSA has been reported earlier [100,104]. The degree of work hardening (UTS/YS) in temperature range of DSA (Table 3.1) is found to be higher in the present investigation.

Table 3.2 Activation energy for DSA in 9Cr–1Mo steel and in the modified 9Cr–1Mo steel and the related processes of DSA.

Material	**Activation Energy (kJ/mol)**	**Authors**	**Remarks**	**Ref.**
9Cr–1Mo steel	83	B.K. Choudhary et al.	DSA process was attributed to carbon	[100,101]
9Cr–1Mo steel	86	B.K. Choudhary	DSA process was attributed to carbon	[20]
Modified 9Cr–1Mo steel	45	R. Kishore et al.	DSA process was attributed to nitrogen	[53]
Modified 9Cr–1Mo steel	64–80	A.K. Roy et al.	varied with silicon content	[50]
Modified 9Cr–1Mo steel	58		DSA process is attributed to nitrogen	Present study

Variation of strain hardening exponent (n), exhibiting peak in the region of DSA, is in agreement with the earlier investigation of Roy et al. [50] for modified 9Cr–1Mo steel. In case of the conventional 9Cr–1Mo steel plateau was observed in temperature range of DSA [105]. However, the values of n at respective temperatures are lower in the present investigation as compared with those reported by Roy et al. [50] and Palaparti et al. [105]. It is relevant to mention that average width of martensite lath was approximately 0.3 μm in the present investigation and this was significantly smaller than those in the earlier investigations [50,105]. Thus, the higher yield strength, tensile strength, and lower strain hardening exponent observed in the present investigation may be understood.

As mentioned in the above section, the minima in ductility in the region of DSA is essentially due to pronounced and rapid drop in necking strain, counteracting even the slight increase in uniform strain (Fig. 3.4b). The drastic and rapid drop in necking strain is due to fall in strain rate sensitivity in the region of DSA (Fig. 3.6). Negative strain rate sensitivity is known to promote flow localization in the form of Luders bands and increased strain hardening enhances the probability of failure at such sites and thereby reducing the ductility [106].

3.8.1.2 Internal Friction

Two peaks in internal friction, so called Snoek peaks, are exhibited in the temperature range 100–250 °C and 300–400 °C (Fig. 3.17). The former peak at lower temperature may be attributed mainly to redistribution of interstitial atoms between octahedral sites in the lattice of ferrite and the latter one at higher temperature to strong interaction between interstitial atoms and dislocations which enhanced the phenomenon of DSA in this temperature range. The appearance of anelastic loss of peak arises mainly due to interaction of dislocations with nitrogen atoms. As carbon atoms have strong interaction with chromium and are strongly bound to Cr atoms and do not induce any measurable anelastic response in this steel [53]. The disappearance of Snoek peak at lower temperature in the 5% and 10% cold worked condition confirm that peak in the normalized and tempered condition results essentially from redistribution of C and N atoms in the ferrite lattice and not from the interaction of solutes and dislocations, in agreement with the earlier observation of Wagner et al. [107]. Since the peak at higher temperature is known to be related to density of mobile dislocations and concentration of interstitial atoms in the vicinity of dislocations, the marked increase in internal

friction above 400 °C may be attributed to enhancement in interaction of solutes with increased density of dislocations, resulting from cold working.

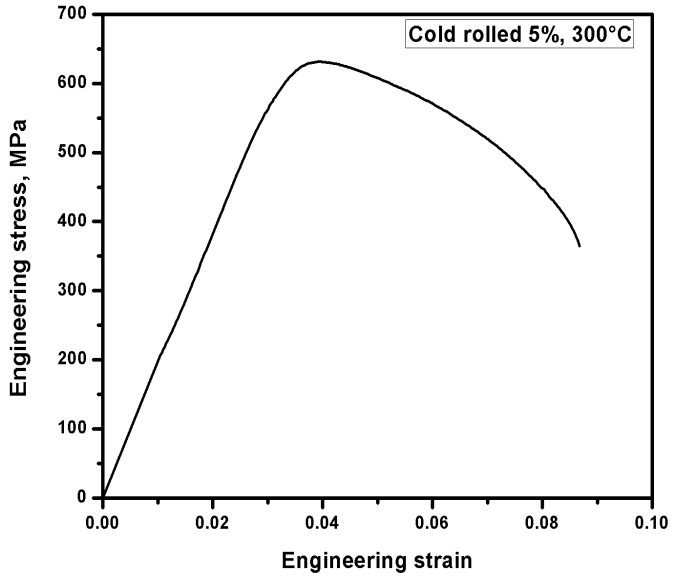

Fig. 3.18. Tensile engineering stress–strain curve of the 5% cold worked modified 9Cr–1Mo steel tested at 300 °C, at strain rate of 10^{-4} s^{-1}, showing smooth curve without serrations.

It may be noted that high temperature Snoek peak is shifted towards higher temperature both in the 5% as well as 10% cold worked condition possibly due to decrease in density of mobile dislocations because of increased interaction between such dislocations. Thus, the shift in Snoek peak to higher temperature in the cold worked condition points to absence of DSA in the temperature range from 250–350 °C which actually is observed in the present investigation. In order to verify further, a tensile test was conducted for the 5% cold worked specimen at 300 °C, at the strain rate of 10^{-4} s^{-1} and the engineering stress–strain curve is shown in Fig 3.18. It may be seen that this curve is quite smooth and free from serrations. Shift of Snoek peak towards higher temperature in the cold worked condition may thus be understood.

3.8.2 Deformation Behavior

Dislocation substructures in the specimens tested at various temperatures from RT to 450 °C revealed distinct differences in configurations of dislocations. There are tangles of high density dislocations at RT (Fig. 3.9). These transformed to distinct subgrains from dislocation cell structure, at 200 °C (Fig. 3.10). From the array of straight dislocations it is obvious that there was no pinning influence on dislocations at 200 °C. In contrast, in the region of DSA, at temperatures of 250 and 350 °C there was formation of dislocation debris (Figs. 3.11 & 3.12). Dislocation arrangement in the laths shows bowing of dislocations resulting from strong pinning of dislocations inside the lattice. In general, dislocation density is observed to be lower in the specimen tested at 200 °C than that tested at RT. In contrast, the relative density of dislocations is increased in the region of DSA at 250 and 350 °C as revealed in Figs. 3.11a & 3.12a respectively. Keller et al. [54] have studied deformation substructures of the modified 9Cr–1Mo steel following uniaxial plastic straining to 1% and 6% at 350 °C, at strain rate of $4 \times 10^{-4}\ s^{-1}$. They observed isolated and piled–up dislocations at 1% plastic strain and high dislocation density and cell structure at 6% plastic strain. However, no dislocation pile–ups were observed in the present investigation.

Irrespective of the test temperature there was tendency for cell formation from 200–450 °C. The cell size formed at 250 °C was found to be smaller and there are pronounced serrations. Cell size is observed to decrease with rise in temperature and remain nearly unchanged from 350 and 450 °C.

The literature related to deformation behavior of modified 9Cr–1Mo steel, particularly in the region of DSA is sparse. At higher temperatures during DSA solute atoms diffuse with higher velocity and form saturated solute atmosphere surrounding the dislocations and thus restrict glide of dislocations. In order to unpin the dislocations

from the atmosphere of interstitial solutes for further deformation, it becomes essential to increase the applied stress which causes high density of dislocations. Formation of bowing of dislocations in the range of DSA (Fig. 3.12) further confirm the increase in stress level and reflect the hindrance caused in freeing of dislocations from solute atmosphere.

3.8.3 Fracture Behavior

There is significant difference in the mode of fracture of the modified 9Cr–1Mo steel from RT to 600 °C, as seen from Figs. 3.14 & 3.15. Rosette type fracture with radial cracks and fibrous zone in the central region are characteristic features of fracture at RT. The detailed investigation of the occurrence of the typical rosette fracture is discussed in the next chapter.

As mentioned in the previous section fibrous zone formed in the range of DSA with equiaxed dimples and there were no facets. The size of the dimples formed at 350 °C is found to be smallest. The contour of dual shear lip zone is seen to be typical in the specimens tested over the temperature range from 200–450 °C and may be associated with mechanical anisotropy in the material. This does not appear to be associated with DSA because it is observed at temperatures even higher or lower than that of DSA.

3.9 Conclusions

The following conclusions are drawn from this chapter:

- There is dynamic strain ageing in the modified 9Cr–1Mo steel over the temperature range from 250–400 °C and serrations of type A, A+B and E are exhibited in plastic flow over the temperature range from 250–350°C, at the strain rate of 10^{-4} s^{-1}.

- Snoek peak in internal friction over the temperature range of DSA further strengthens the occurrence of DSA.
- Activation energy of the process of DSA is estimated to be 58 kJ/mol, which is equivalent to activation energy for diffusion of nitrogen atoms in ferrite matrix. Thus nitrogen in this steel is identified to play major role in the process of DSA
- There is formation of dislocation cell structure from rearrangement of dislocations over the temperature range from 200 and 450 °C. Other typical features of dislocations; like bowing and loop formation were also observed in the region of DSA.
- There is typical ductile fracture with fibrous zones without facets and formation of double shear lip zones in the temperature range from 200–450 °C.